The Extension of Endmember Extraction to Multispectral Scenes

John Gruninger[*a], Anthony J. Ratkowski[b], and Michael L. Hoke[b]

[a]Spectral Sciences Inc., 4 Fourth Avenue, Burlington, MA 01803, USA
[b]AFRL/VSBYH, 29 Randolph Road, Hanscom AFB, MA 01731, USA

ABSTRACT

A multiple simplex endmember extraction method has been developed. Unlike convex methods that rely on a single simplex, the number of endmembers is not restricted by the number of linearly independent spectral channels. The endmembers are identified as the extreme points in the data set. The algorithm for finding the endmembers can simultaneously find endmember abundance maps. Multispectral and hyperspectral scenes can be complex and contain many materials under a variety of illumination and environmental conditions, but individual pixels typically contain only a few materials in a small subset of the illumination and environmental conditions which exist in the scene. This forms the physical basis for the approach that restricts the number of endmembers that combine to model a single pixel. No restriction is placed on the total number of endmembers, however. The algorithm for finding the endmembers and their abundances maps is sequential. Extreme points are identified based on the angle they make with the existing set. The point making the maximum angle with the existing set is chosen as the next endmember to add to enlarge the endmember set. The maximum number of endmembers that are allowed to be in a subset model for individual pixels is controlled by an input parameter. The subset selection algorithm is sequential and takes place simultaneously with the overall endmember extraction. The algorithm updates the abundances of previous endmembers and ensures that the abundances of previous and current endmembers remain positive or zero. The method offers advantages in multispectral data sets where the limited number of channels impairs material un-mixing by standard techniques. A description of the method is presented herein and applied to real and synthetic hyperspectral and multispectral data sets.

Keywords: hyperspectral, multispectral, endmember, un-mixing, simplex

1. INTRODUCTION

We have developed convex factorization techniques that can automatically generate sets of endmember spectra for hyperspectral and multispectral imagery. Linear mixing models and endmember abundances are determined simultaneously with endmember extraction. The method is based on techniques developed for hyperspectral scenes[1]. The addition of constraints on the number of endmembers allowed in single-pixel mixing models enables application of the method to the extraction of larger numbers of endmembers from multispectral scenes.

Typical scenes may contain many materials and each material will have spectral variability. Even after atmospheric correction, environmental and illumination effects still persist in the data and more than one spectrum is typically required to describe a material. The number of materials and their spectral variations may exceed the rank of the data sets, the number of linearly independent channels. The standard linear mixing model is based on a set of material spectra or endmember spectra chosen to model the scene. Each pixel is modeled using the set as a basis. The basis must be linearly independent and its dimension is dictated by the rank of the endmember spectra rather than by the number of materials and spectral variations that are present in the data. This limitation leads to poor estimates of material abundances when a basis is inadequate to represent the material and its spectral variations. A collection of local models, each describing a small number of materials and their environmental variations, would provide a more desirable description of a scene. Strategies have recently been developed for determining abundances when a set, or 'bundle', of spectra is used to describe each material. These include a linear programming technique[2], a regularized constrained least-squares approach[3] and a stochastic mixing model approach[4]. Alternatively, stepwise constrained least-squares approaches can be used to select subsets of endmember spectra to model each pixel spectrum[5,6]. These linear programming and least-squares procedures require the existence of an adequate set of endmember spectra that describes the scene materials and their spectral variability.

---

[*] john@spectral.com; phone 1 781 273-4770; fax 1 781 270-1161; www.spectral.com

Several endmember extraction procedures have been developed. Autonomous algorithms include ORASIS[7], N-FINDR[8] and Iterative Error Analysis (IEA)[9]. These algorithms were compared recently[10]. They were also compared to the interactive pixel purity index method[11]. ORASIS is a suite of codes that can find endmembers from a scene autonomously. It uses a Modified Gram- Schmidt (MGS) algorithm to factor the data matrix, and then a shrink-wrapping technique is used to find an outer simplex[12,13] that encloses the data. The extreme points of the outer simplex need not be data points. After the endmembers have been found, a constrained linear mixing model can be used to obtain material abundance maps. Alternatively, to maintain speed for real-time processing, ORASIS has the option of skipping the shrink-wrapping, using the vectors selected by the MGS procedure and a set of filter vectors[14] derived from unconstrained least squares. In this mode, the ORASIS procedure finds an orthogonal basis to fit the data. Our MGS method is similar to the ORASIS mode when shrink-wrapping is not applied. N-FINDR is an endmember code that runs autonomously and finds pure pixels that can be used to describe the mixed pixels in the scene. The algorithm finds an inner simplex within the data and selects the largest volume simplex. After the endmember determination step, N-FINDR uses a constrained linear mixing model to obtain abundances. The IEA approach performs a sequence of constrained un-mixings, starting with the data spectrum that is least well modeled by the average and selecting additional endmembers from the most poorly modeled data spectra at each step. At each step a simplex is formed from the selected data spectra. The process terminates when the number of endmembers sought are found or a selected tolerance on residual error has been met. The selection of extreme vectors in our factorization procedure is very similar to the IEA approach. The distinction is the limitation of IEA to finding linearly independent endmembers. All of these methods find linear-independent sets of spectra as endmembers. The pixel abundances are obtained after selection via a common linear mixing model for all pixels. Many hyperspectral data sets and most multispectral data sets contain more extreme spectra than the rank of the data. For such cases, these endmember procedures find and utilize only a subset of the extreme spectra in the data.

The convex factorization method determines extreme spectra and abundances simultaneously. The abundance matrices are sparse, with pixels of similar scene materials being described by the small subsets of the endmembers. Each subset forms its own convex span, leading to a description of hyperspectral or multispectral data in terms of multiple sets of convex cones or simplices with one set for each material or mix of materials. While the complete set of endmembers may be linearly dependent, the subsets in hyperspectral scenes are typically linearly independent. Because of the natural tendency toward sparse representation, with only a few endmembers per pixel, enforcing a maximum allowed number of endmembers per pixel to ensure linear independence affects the modeling of only a small number of pixels. Constraining the maximum number of endmembers per pixel model to a value less than or equal to the rank guaranties that linearly-independent models are obtained. We have added this constraint to our convex factorization procedures. For multispectral applications, the total number of endmembers found can substantially exceed the number of spectral channels available. The maximum dimension of the subsets can be controlled to ensure that a well-conditioned model is obtained for each pixel and material type, while the total basis size is based on scene complexity and variability.

A description of the matrix factorization techniques is given in Section 2. In Section 3 the new method is compared with the Sequential Maximum Angle Convex Cone (SMACC) endmember extraction algorithm[1] by applying both to a moderately complex AVIRIS hyperspectral scene of the Harrisburg Pennsylvania airport. Finally, the capabilities for endmember and abundance map extraction in multispectral scenes are illustrated by applying the approach to a synthetic LANDSAT scene of the Harrisburg airport- using the six visible and near-IR LANDSAT channels.

2. METHOD

Endmembers of the hyperspectral or multispectral data sets are obtained by seeking a basis of 'extreme vectors'. 'Extreme vectors' are unique vectors having the property that they cannot be approximated by positive linear combination of other vectors belonging to the data set. 'Non-extreme vectors' can be approximated by a positive linear combination of the extreme vectors. The convex factorization procedure uses a sequential convex cone strategy[1] to find extreme vectors with the number of extreme vectors increasing until an acceptable threshold residual is reached or a pre-specified number of extreme vectors has been found. A convex cone expansion requires that the expansion coefficients are positive, while a convex hull expansion additionally requires that the expansion coefficients for the spectrum or image model sum to one.

2.1 Linear expansion of MSI/HSI data

Hyperspectral and multispectral data are given a matrix representation, H, by assigning scene pixel spectra to its columns. The element, $H_{i,j}$, is the radiance in the ith channel of the jth pixel. Given the high redundancy in the data, the matrix can be expressed by a convex factorization:

$$H_{i,j} = \sum_{n}^{N} S_{i,n} F_{n,j}^{N} + R_{i,j}^{N} \text{, with the constraints } F_{n,j}^{N} \geq 0. \tag{1}$$

The N columns of S are the spectral endmembers. F^{N} is a matrix of expansion coefficients. It contains the contribution of each endmember to each pixel. The matrix R^{N} is the error or residual matrix resulting from truncation of the expansion to a set of N endmembers. In convex factorization, the majority of pixels are modeled by only a few of the basis functions and the majority of expansion coefficients are zero. To accurately model complex scenes with a large number of materials and environment and illumination variations, a large number of endmembers is required. With multispectral data, the number of materials and environmental variations can far exceed the number of channels of data, making standard linear mixing impossible. To have both spectral variability in the basis set and numerical stability, the number of basis functions per pixel model is restricted to a number, L, that is less than or equal to the rank, while the total number of endmembers, N, may exceed the rank. By defining an indexing array, b, whose elements, $b(l, j)$, indicate the lth endmember in the model of the jth pixel, the expansion can be expressed as

$$H_{i,j} = \sum_{l}^{L} S_{i,b(l,j)} G_{l,j}^{N} + R_{i,j}^{L,N} \tag{2}$$

with constraints

$$G_{l,j}^{N} \geq 0 \, .$$

Here a maximum of L endmembers from the set of N are used to model each pixel. The matrix G^{N} contains the expansion coefficients of the L endmembers for the models of each pixel. The restriction to a maximum of L endmembers leads to the subset selection problem: find the best L endmembers out of the set of N endmembers to model a pixel spectrum. Optimum solutions to the subset selection problem have high combinatorial complexity and are computationally prohibitive for reasonably- sized endmember sets. Stepwise procedures provide an alternative (suboptimal) solution, where the best endmember to add to the current set is selected for each pixel at each step. Both of these techniques require the existence of the endmember basis prior to modeling. They focus on the best model for each pixel individually.

The approach taken here is a suboptimal method that focuses on the modeling of the entire scene. There are two subset selection problems to be solved. First, the selection of N endmembers from the data set and, second, the selection of the subset of L endmembers from the total set of N to model each pixel. The processes of determination of the basis of N endmembers and the selection of L or fewer of them for each pixel model are performed simultaneously in a sequential procedure. The endmember selection is based on the reduction of residuals in the modeling of the entire scene. As each new endmember is selected, all pixel models are updated. Update options include either adding the new endmember to the pixel model or leaving the pixel model unchanged. When the new endmember is added, it either enlarges the size of the pixel basis subset or maintains the size by replacing a prior endmember. The replacement option reduces the dependency of the models on the order of selection. The selected endmembers are extreme vectors within the data. The subsets of the endmembers that model pixel spectra are convex sets. The subsets can provide multiple convex cone or simplex models for the scene.

The method is based on the expansions expressed in Equations 1 and 2. The set of endmembers $\{s_n\}$ that form the matrix S are selected from the columns $\{h_j^0\}$ of H. The initial vector from the set $\{h_j^0\}$ can be selected by several criteria. We choose it to be the longest vector, which corresponds to the brightest pixel in the scene. Subsequent endmembers are selected as the pixel spectra that are the most poorly modeled with the current endmember set. The

n^{th} endmember is the pixel spectrum with the largest residual norm in the n-1 endmember set. After selection of the new endmember, the pixel models are updated by oblique projection. The array, q, is used to store the column indices of the data matrix that are chosen to form the columns of S, $\{s_n = h^0_{q(n)}, 1 \le n \le N\}$.   A set of auxiliary vectors, $\{w_n, 1 \le n \le N\}$ are used in the processing. The index of the selected vector is stored in $q(n)$ and the auxiliary vector, w_n, is defined as $w_n = h^{n-1}_{q(n)}$. The projection process forms the set of vectors $\{h^n_j\}$ and oblique projection coefficients $F^n_{n,j}$, for $n=1,N$, as

$$h^n_j = h^{n-1}_j - w_n F^n_{n,j}$$

with

$$F^n_{n,j} = \alpha_{n,j} O_{n,j} = \alpha_{n,j} \frac{(w_n \mid h^{n-1}_j)}{(w_n \mid w_n)}$$

(3)

The $O_{n,j}$ are orthogonal projection coefficients. The parameters $\alpha_{n,j}$ are selected so the oblique projections force the expansion to satisfy the positivity constraints and the total limit on the number of basis functions permitted per pixel model. The lengths of the vectors h^n_j are the residual norms for the approximation of the vectors with the basis set of n vectors. The expansion coefficients are obtained and updated for the nonorthogonal basis at each selection and projection step. We introduce the coefficient notation, $F^n_{k,j}$, and the value of the expansion coefficient of the kth basis vector in its expansion of the jth column of H after its update on entry of the nth endmember to the set. When $k = n$, the coefficient is the oblique projection coefficient given by Equation 3. For $k < n$, $F^n_{k,j}$ is an updated expansion coefficient of the kth previously selected endmember. Updates to the expansion coefficients on entry of the nth endmember to the basis are given by

$$F^n_{k,j} = F^{n-1}_{k,j} - F^{n-1}_{k,q(n)} F^n_{n,j},$$

(4)

where $F^{n-1}_{k,q(n)}$ is the expansion coefficient in the approximation of w_n by the previously selected k^{th} endmember. For $F^n_{k,j} \ne 0$, the index array and expansion coefficient array for the pixels are updated. The index l is determined, and then the index array and the expansion coefficients are set as

$$b(l, j) = k \text{ and } G^n_{l,j} = F^n_{k,j}.$$

(5)

The process is continued until after N endmembers are found, or all of the residual norms of the pixel spectra are below an acceptable threshold. At termination, the expansion coefficients of the selected endmembers are updated to

$$G^N_{1,q(n)} = 1 \text{ and } G^N_{l,q(n)} = 0, \text{ for } 2 \le l \le L.$$

(6)

The final set of coefficients $\{G^N_{l,j}\}$ are the elements of the expansion matrix of Equation (2). The set of vectors $\{h^N_j\}$ form the columns of the residual matrix, $R^{L,N}$.

2.2 Selection of oblique projections

The oblique projections form the foundation of the approach. For positive data, such as spectra, the first endmember taken from the data will have a positive orthogonal projection coefficient with all of the other pixel spectra. The initial values of the expansion coefficients for the first endmember are the orthogonal projection coefficients. For $n > 1$, the

previous expansion coefficients have to be updated for the nonorthogonal basis and oblique projections are required to satisfy active constraints.

The constraints are maintained in the sequential process by the selection of the $\alpha_{n,j}$ parameters to define the oblique projections. First the orthogonal projection coefficient, $O_{n,j}$, is found. It is modified, as necessary, changing the projection to an oblique projection, to satisfy the constraints using the following procedure:

1. If the orthogonal projection coefficient is not positive, this endmember cannot contribute to a convex model of this data vector and the expansion coefficient is set to zero:
    If $O_{n,j} \leq 0$, set $\alpha_{n,j} = 0$ and $F_{n,j}^n = 0$.

2. If the orthogonal projection coefficient is positive, then an oblique projection is sought. If none of the updates in Equation 4 leads to a negative coefficient, no positive constraints are active. If one or more of the updated coefficients would become negative, if the orthogonal projection is used, a positive constraint is active. An oblique projection is used instead of the orthogonal projection. The result is the removal of a previously selected endmember for the model. The steps are

    (a) Find the smallest value, $v_{\min}$, of the set

    $$\{v_k = \frac{F_{k,j}^{n-1}}{F_{k,q(n)}^{n-1} O_{n,j}}\} \text{ for all previous extreme vectors}, 1 \leq k \leq n-1, \text{ in the model of the new endmember, } q(n).$$

    (b) If $v_{\min} \leq 1$, then a positive constraint is active. The end-spectrum, s_k, with $v_k = v_{\min}$ will be removed from the convex model of pixel. Set $\alpha_n = v_{\min}$. The oblique projection coefficient is set to $F_{n,j}^n = \alpha_{n,j} O_{n,j}$.

    (c) If $1 < v_{\min} < 2$ then no positive constraint is active. However an oblique projection can be performed that will simultaneously replace the endmember, s_k, with $v_k = v_{\min}$, and simultaneously lower the residual. As illustrated in Figure 1, the length of the residual vector will be reduced, $|h_j^n| < |h_j^{n-1}|$, for all $\alpha_{n,j}$ satisfying $0 < \alpha_{n,j} < 2$. If the current model size for pixel j is at its maximum, set $\alpha_{n,j} = v_{\min}$ and $F_{n,j}^n = O_{n,j}$. If the current model size is less than the maximum, the orthogonal projection coefficient will lead to the greatest lowering of the residual. Set $\alpha_{n,j} = 1$ and $F_{n,j}^n = O_{n,j}$.

    (d) If $v_{\min} \geq 2$, no positive constraint is active, and no replacement is possible with a simultaneous reduction in residual. If the current model size is less than the maximum, use the orthogonal projection. Set $\alpha_{n,j} = 1$, and $F_{n,j}^n = O_{n,j}$. If the current model size is at the maximum, this endmember will not be used to model this pixel. Set $\alpha_{n,j} = 0$ and $F_{n,j}^n = 0$.

The previous expansion coefficients are updated using Equation 4 and the value of $F_{n,j}^n$ selected. Geometrically, when a positive constraint is active, the projection is oblique with $\alpha_{n,j} \leq 1$, as illustrated in Figure 1. With the replacement option active, the projection is oblique with $1 < \alpha_{n,j} < 2$. The lengths of the residual vectors for the orthogonal (solid vertical line) and oblique projections (dashed line and dotted line) are smaller than the previous residual vector with the unconstrained orthogonal projection leading to the smallest residuals. The convex projection will be as close as possible to the orthogonal projection while maintaining the positive constraints and the basis set size constraint. It differs from the orthogonal projection only when one of these constraints is active. An active constraint leads to one of the previous extreme vectors being removed from the expansion. If no constraints are active, the orthogonal projection is used and the new extreme vector is added to the description of the data vector with no prior one being removed.

$$h_j^{n-1}$$

$$h_j^n$$

$$h_j^n$$

$$W_n \qquad \alpha_{n,j}O_{n,j} \qquad O_{n,j} \qquad\qquad \alpha'_{n,j}O_{n,j}$$

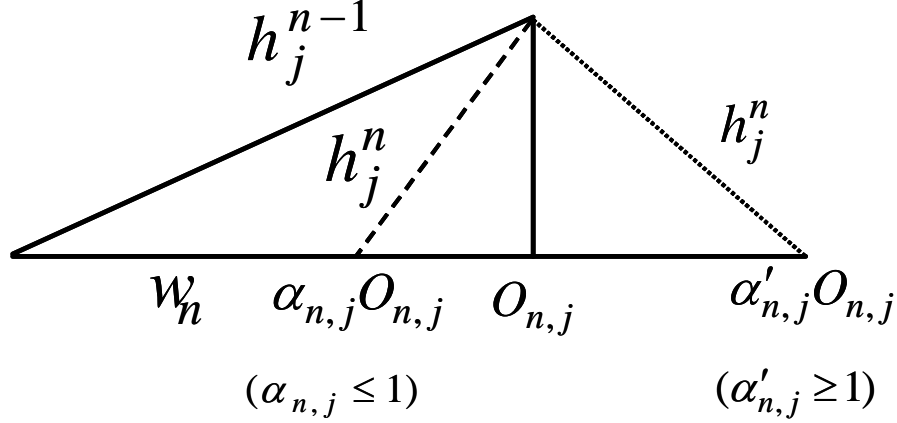$$(\alpha_{n,j} \leq 1) \qquad\qquad (\alpha'_{n,j} \geq 1)$$

Figure 1. Illustration of oblique projection and orthogonal projection. For $(0 < \alpha_{n,j} < 2)$ the resulting residual vector is shorter than the residual of the previous step, with the largest reduction for, $(\alpha_{n,j} = 1)$, the orthogonal projection. $\alpha_{n,j}$ is selected to be less than one to satisfy active constraints on positivity and force removal of a previous endmember. $\alpha_{n,j}$ is selected to be larger than one to replace a previous endmember.

The convex factorization results differ from those of the unconstrained factorization in several ways. The vectors, $w(n)$, obtained in the convex factorization do not form an orthogonal set. The expansion coefficients are not the optimal constrained least-squares expansion coefficients. They are stepwise-constrained least-squares coefficients. The set of vectors, $\{s_n\}$, are a set of extreme vectors of the data set. Several of the columns selected will differ from those obtained for the orthogonal case. The extreme vectors need not be linearly independent. In general, there are more extreme points in a data set than the rank. Our algorithm is often stable when the rank is exceeded since the expansion coefficients are computed simultaneously and the pixel spectra are computed using a subset of the basis. Numerical problems occur only if the dimension of the subset selected to model an individual pixel spectrum exceeds the rank. The procedure specifically avoids this possibility.

3. APPLICATIONS

In this Section three applications of the methods are described. First, the method is applied to a hyperspectral data set, with and without a constraint on the number of endmembers that can contribute to a pixel model. An AVIRIS scene of the Harrisburg Pennsylvania airport is used for the comparison. In addition, a synthetic LANDSAT scene, derived from the AVIRIS Harrisburg airport scene, was processed to illustrate the capabilities of the new convex techniques for multi-spectral imagery. These results are compared to similar processing of the full 224-channel AVIRIS scene.

3.1 AVIRIS Harrisburg airport scene
An AVIRIS Harrisburg airport data set was selected as a test case. It is moderately complex and has several material types spatially resolved. An image is shown in Figure 2. The scene is a 401x401 pixel array. The full data set contains 224 AVIRIS spectral channels from approximately 0.4 μm to 2.5 μm. We used the data directly with no atmospheric correction. We have studied the scene previously in an effort to determine the compression capabilities of our convex factorization methods. The pixel spectra of the scene were first normalized so that their integrated intensity was unity. This keeps the endmember selection process from favoring the brightest pixels over those that are spectrally most different. The pixel selected as the first endmember, however, was the brightest pixel in the scene. Two calculations were performed on the Harrisburg AVIRIS scene with the full 224-channels. One of the calculations constrained the abundances to be positive or zero, but placed no constraint on the number of endmembers that could be used to describe a pixel. In the second calculation, the number of endmembers that could model a pixel was constrained to be less than or equal to 6.

In the first calculation, the first one hundred endmembers were found. It was determined that fewer than 20 of the endmembers contribute to more than 5 % of the pixel models. The remaining endmembers model small localized objects, or a scattering of tiny isolated points. These are of interest for anomaly detection. We used the residual norm, the length of the residual vector to the pixel models, as a measure of the quality of the endmember models. The least-well-modeled pixel has the largest residual norm. In this case, the maximum residual norm was 0.010 or 1 % of the worst-case pixel's original length. The average residual norm for all modeled pixels was 0.0032. Of the pixel models, the most common contained contributions from 1 to 6 endmembers with more than 62 % modeled with fewer than 7 endmembers. Less than 1 % of the pixel models included more than 10 endmembers. The pixels that were modeled with a large number of endmembers typically had only minimal contributions from several of the endmembers in the model. If the endmembers with abundances of less than .05 are ignored, no pixels have contributions from more than 9 endmembers and only 1 % of the pixel models exceed 6 endmembers. Over 68 % of the pixel models contain four or fewer endmembers with abundances greater than 0.05.

Figure 2. Composite of AVIRIS Harrisburg airport scene

The second calculation with the full 224-channel AVIRIS scene differed from the first in that the pixels models were constrained to a maximum of six endmembers. The first 100 endmembers were found. The endmembers found were identical in both pixel location and order of selection for the constrained pixel model calculation and the unconstrained calculation. The maximum residual norm, 0.011, and the average residual norm, 0.0033, were only slightly larger than those for the unconstrained case. This indicates that when the constraint is active, the surviving endmember abundances are adjusted by the algorithm to compensate for the reduced number of endmembers in the pixel model. The penalty for applying a maximum model size constraint for pixel spectra is quite small. This is a general result. For most pixels in a scene, a maximum model constraint will not be active. The remaining small percentage of the total pixels will be adequately modeled within the constraints in a scene.

3.2 Multi-spectral application
To investigate the capability of the method for multispectral scenes, a synthetic multispectral scene was generated from the Harrisburg AVIRIS scene using the six VIS-NIR channels of the LANDSAT sensor. The synthetic LANDSAT scene has the same spatial resolution as the AVIRIS scene. Again, the first 100 endmembers were sought, under the constraints of positive or zero abundance and a maximum of six endmembers in a pixel model. As a preprocessing step, the synthetic LANDSAT scene was also normalized so that the integrated intensity over all six bands was unity. The first endmember, selected as the brightest pixel, was the same pixel as in the full 224-channel cases. Of the remaining endmembers, several which were ubiquitous in pixel models were either selected as identical, adjacent or nearby pixels to those chosen in the full 224-channel calculations. However they were not chosen in the same order. In other cases, different pixels were chosen but the endmember spectra and the endmember abundances were very similar. In all, fifteen of the major endmembers and their abundances for the 224-channel calculations were found to be highly correlated with fifteen of the major endmembers of the 6-channel calculations.

In our comparisons, we concentrate on spatial information that is made available via the endmember abundance maps and illustrate similarities between the abundance maps and the spectral features of the endmembers. The major endmembers are those that are selected early in the processing and those that are selected later but are contained in several pixel models. Together, they describe the main features of the scene. We found fifteen endmember pairs, one in

the 224-channel image and one in the 6-channel image, that have highly correlated spectra and abundance maps. The first four of the fifteen pairs contain the first four endmembers selected by the 224-channel and 6-channel calculations. The order of selection differs beyond that for the two calculations. The fifth endmember pair contains the fifth endmember selected by the 6-channel calculation and the seventh endmember of the 224-channel calculations. For the first eight endmember pairs, the pixels selected as endmembers in the two calculations are either identical or adjacent. For the remaining pairs, the pixel locations are not adjacent, but the spectra are similar as are the abundance maps.

The spectra and abundance maps for fifteen endmember pairs are illustrated in Figures 3 to 17. Figure 3a and 3b contain the abundance maps for the first endmember pair for the full 224-channel scene and the 6-channel synthetic LANDSAT scene, respectively. The brightest pixel, (182,170) was chosen as the first endmember in both scenes; it is located on an aircraft in the center of the scene. The abundance maps for this endmember for the 224-channel and 6-channels scenes are very similar. In addition to other aircraft pixels, this endmember also contributes to pixel models of a central rooftop and other rooftops, and to a lesser extent to the paving and the tarmac. The scale is linear from dark to light representing abundances between 1 and 0, respectively. The 224- and 6-channel spectra of the endmember are shown in Figure 3c. The abundance maps Figures 4a and 4b contain the abundance maps for the second endmember pair. Again the maps are very similar and define regions of vegetation. The endmember selected in both cases is a pixel in the lower left corner of the scene, (27,388). The spectra for this endmember pair are illustrated in Figure 4c. Abundance maps for the third endmember pair and its spectrum are shown in Figures 5a, 5b and 5c. The pixel location of the endmember in the 224-channel calculation is (247,24) while the pixel selected by the 6-channel calculation was (245,24). These are two, nearly adjacent, spectrally similar pixels in the upper central region of the scene. They are both in a region that is shaded by a building. The endmembers contribute to several pixels that are shadowed by objects in the scene. Those near the aircraft are not aircraft pixels but rather the shaded tarmac, and similarly pixels modeled in the parking lot are in shaded areas. The endmember contributes to more pixel models in the LANDSAT scene, primarily on the right side of the image. Figures 6a and 6b contain the abundances of the fourth endmember pair. The same pixel (210,290) was selected by both the 224-channel and 6-channel calculations. The endmember spectra are illustrated in Figure 6c. From the visible portion of the spectra, it can be seen that the pixel is a red object, located on a drive or road to the right of a large light-colored building. This pixel contributes to the models of other red-colored objects in the parking lot as well as contributing to the modeling of the tarmac and an area of bare ground above the large parking lot. This endmember plays a larger role in modeling the tarmac in the 224-channel scene than in the 6-channel scene although it is minor constituent in the tarmac modeling. The abundance maps for the fifth endmember pair are illustrated in Figures 7a, and 7b. The same pixel was chosen in both calculations (329,352). This pixel is an object in the upper central area of the parking lot in the lower right region of the scene. The pixel contributes to the models of paving and rooftops and other objects in the parking lot. The pixel contributes more strongly to the fully illuminated left side of a long narrow building on the upper right of the scene in the 224-channel calculations and it contributes to the modeling of the partially illuminated right side of the roof of the cargo storage building across the street. The pixel does not contribute to the modeling of the cargo storage building roof in the six-channel model. The spectra of the endmember pair are illustrated in Figure 7c. The abundance maps for a sixth endmember pair are illustrated in Figures 8a and 8b. A common pixel (204,2) at the top and center of the scene was selected by the two calculations. The abundance maps are again similar overall; however, there are differences. The pixel is used as a major contributor to the model of the structure in the lower right of the scene, to the right of the parking lot, in the 6-channel calculations and contributes more strongly to the area at the edge of right side of the cargo storage building. The spectra for this endmember pair are illustrated in Figure 8c.
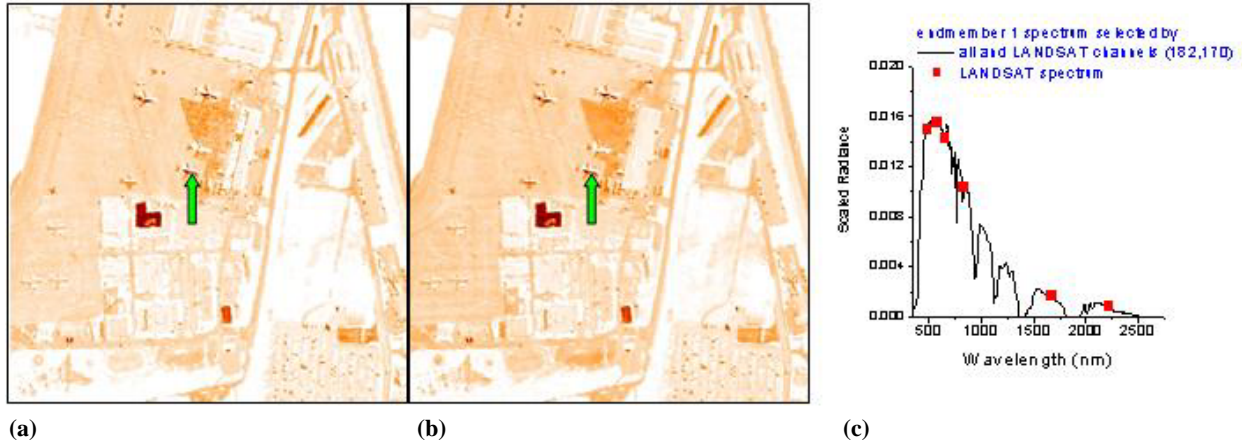
(a) **(b)** **(c)**

Figure 3. Abundance maps derived from the full 224-channel calculations and the 6-channel calculations for endmember pairs (1) are in Figures 3a and 3b, respectively. Arrows on the abundance maps point to pixel locations of the selected endmembers. The normalized radiance spectra of the endmember pairs are shown in Figure 3c.
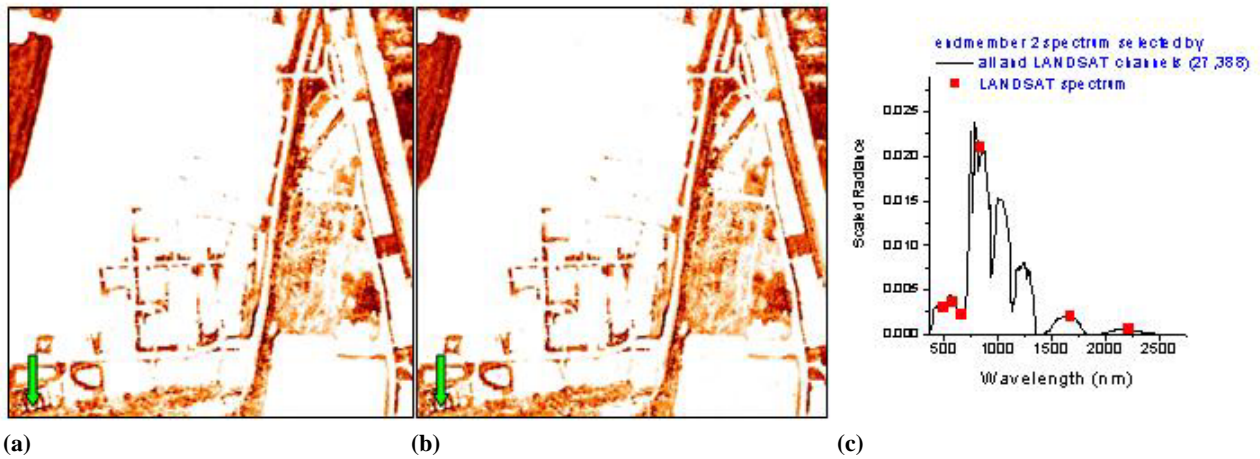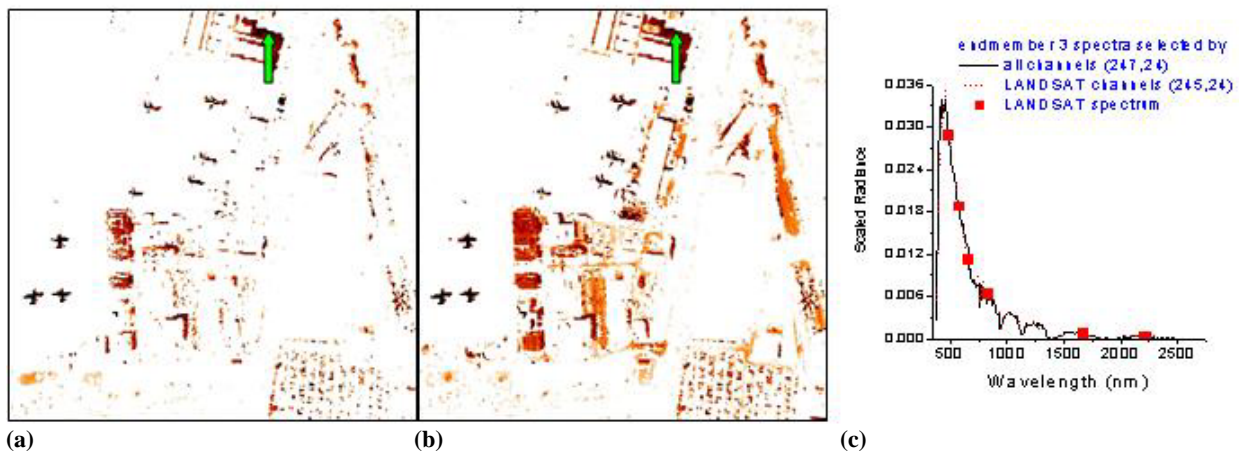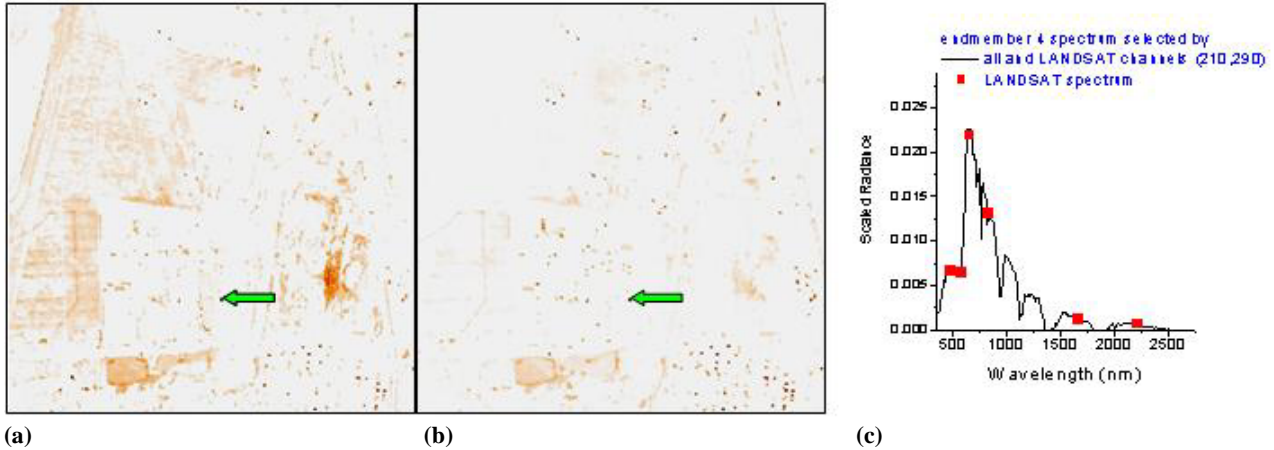

(a) **(b)** **(c)**

Figure 4. Abundance maps derived from the full 224-channel calculations and the 6-channel calculations for endmember pairs (2) are shown in Figures 4a and 4b, respectively. Arrows on the abundance maps point to pixel locations of the selected endmembers. The normalized radiance spectra of the endmember pairs are shown in Figure 4c.
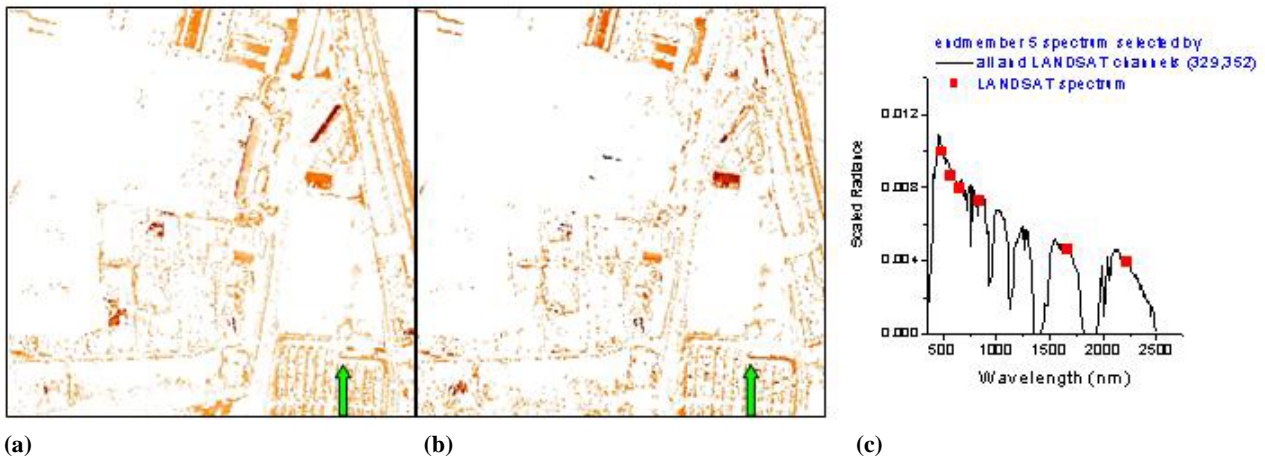

(a) **(b)** **(c)**

Figure 5. Abundance maps derived from the full 224-channel calculations and the 6-channel calculations for endmember pairs (3) are shown in Figures 5a and 5b, respectively. Arrows on the abundance maps point to pixel locations of the selected endmembers. The normalized radiance spectra of the endmember pairs are in Figure 5c.

(a)   **(b)**   **(c)**

Figure 6. Abundance maps derived from the full 224-channel calculations and the 6-channel calculations for endmember pairs (4) are shown in Figures 6a and 6b, respectively. Arrows on the abundance maps point to pixel locations of the selected endmembers. The normalized radiance spectra of the endmember pairs are in Figure 6c.
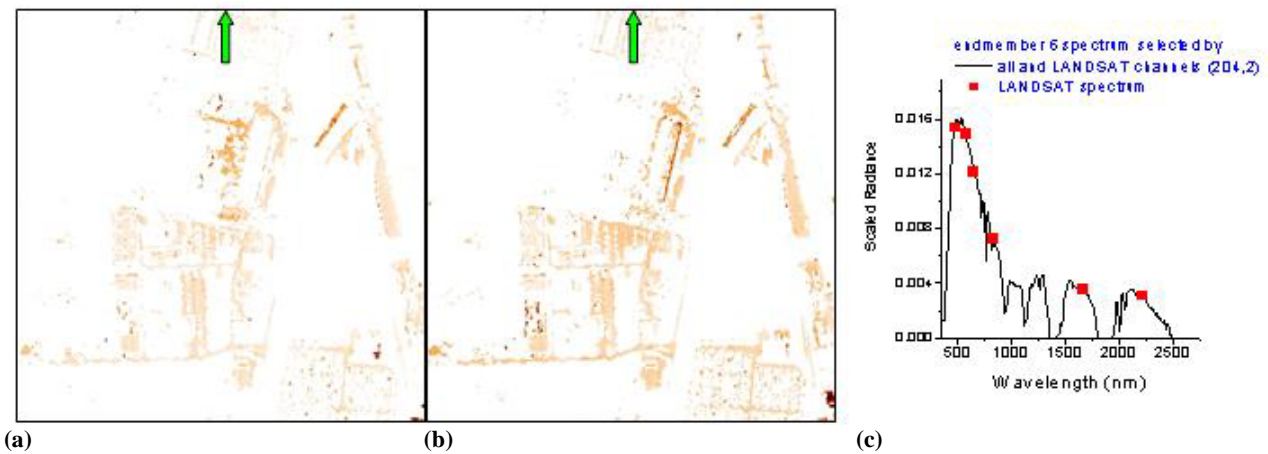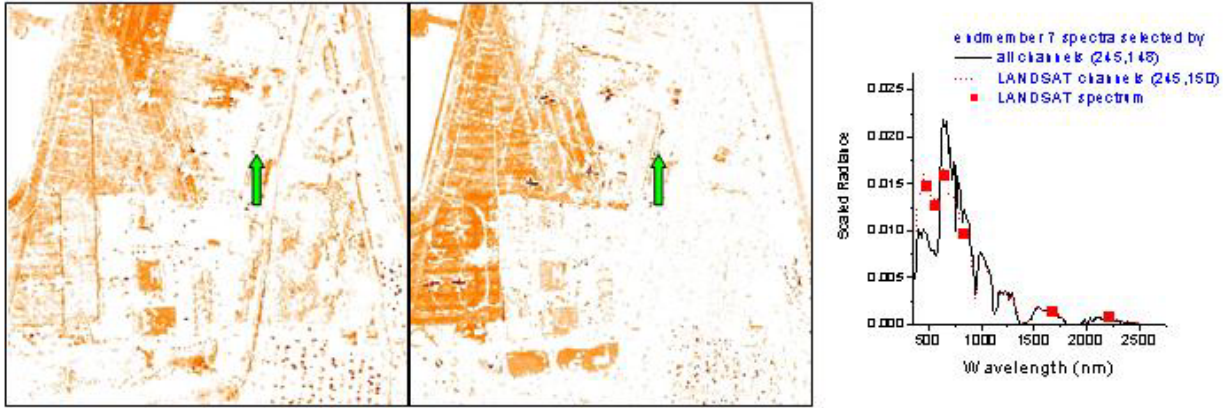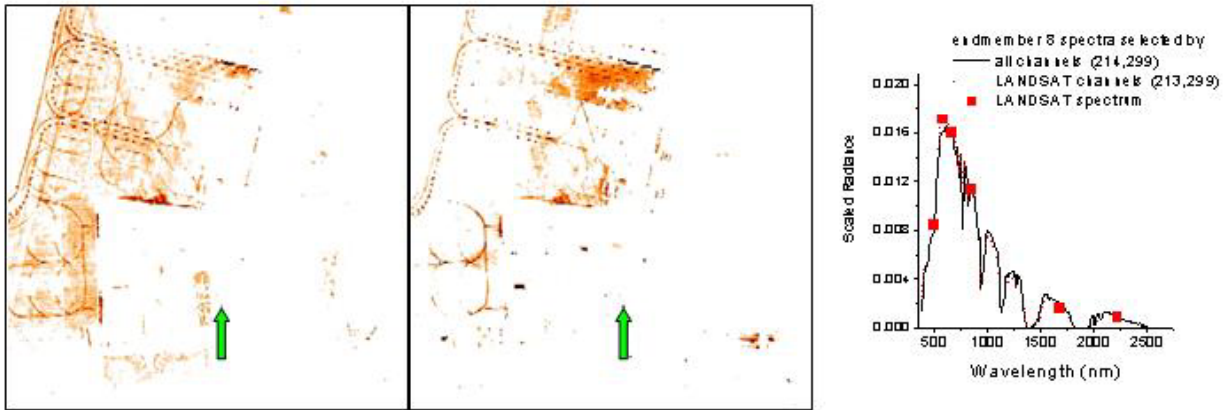

(a)   **(b)**   **(c)**

Figure 7. Abundance maps derived from the full 224-channel calculations and the 6-channel calculations for endmember pairs (5) are in Figure 7a, 7b respectively. Arrows on the abundance maps point to pixel locations of the selected endmembers. The normalized radiance spectra of the endmember pairs are in Figure 7c
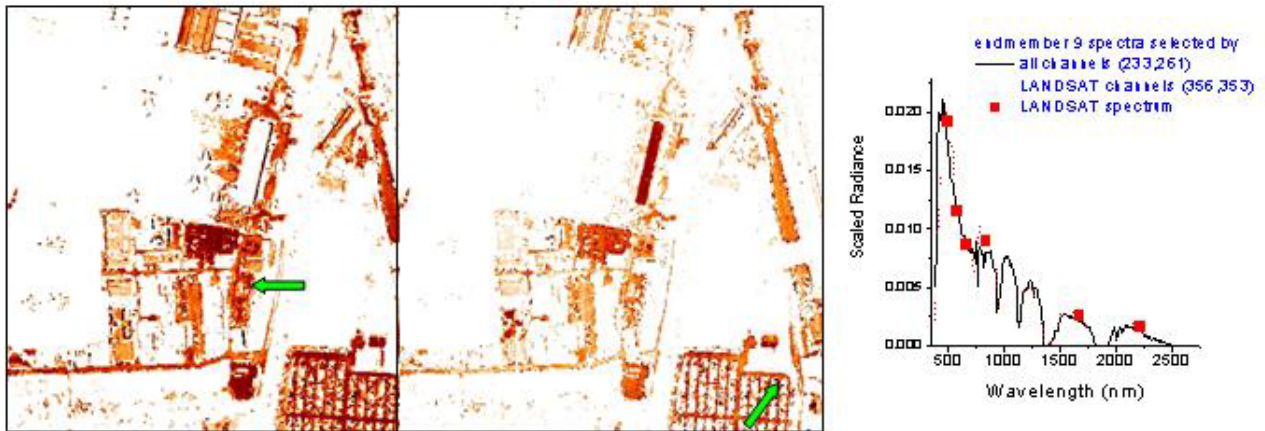

(a)   **(b)**   **(c)**

Figure 8. Abundance maps derived from the full 224-channel calculations and the 6-channel calculations for endmember pairs (6) are in Figure 8a, 8b respectively. Arrows on the abundance maps point to pixel locations of the selected endmembers. The normalized radiance spectra of the endmember pairs are in Figure 8c.

(a)   **(b)**   **(c)**

Figure 9. Abundance maps derived from the full 224-channel calculations and the 6-channel calculations for endmember pairs (7) are in Figure 9a, 9b respectively. Arrows on the abundance maps point to pixel locations of the selected endmembers. The normalized radiance spectra of the endmember pairs are in Figure 9c.

(a)   **(b)**   **(c)**

Figure 10. Abundance maps derived from the full 224-channel calculations and the 6-channel calculations for endmember pairs (8) are in Figure 10a, 10b respectively. Arrows on the abundance maps point to pixel locations of the selected endmembers. The normalized radiance spectra of the endmember pairs are in Figure 10c.

(a)   **(b)**   **(c)**

Figure 11. Abundance maps derived from the full 224-channel calculations and the 6-channel calculations for endmember pairs (9) are in Figure 11a, 11b respectively. Arrows on the abundance maps point to pixel locations of the selected endmembers. The normalized radiance spectra of the endmember pairs are in Figure 11c.
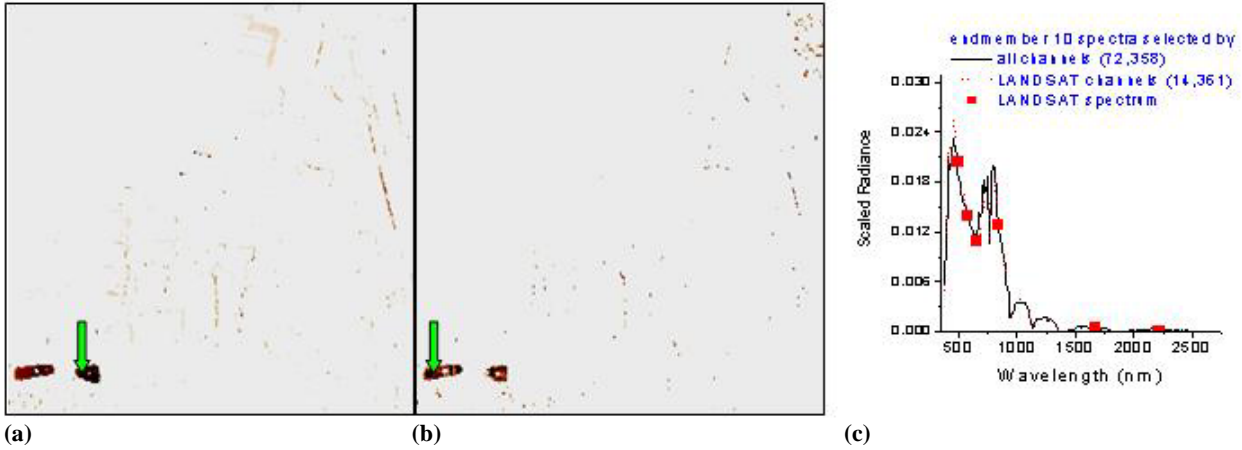
(a)   **(b)**   **(c)**

Figure 12. Abundance maps derived from the full 224-channel calculations and the 6-channel calculations for endmember pairs (10) are in Figure 12a, 12b respectively. Arrows on the abundance maps point to pixel locations of the selected endmembers. The normalized radiance spectra of the endmember pairs are in Figure 12c.

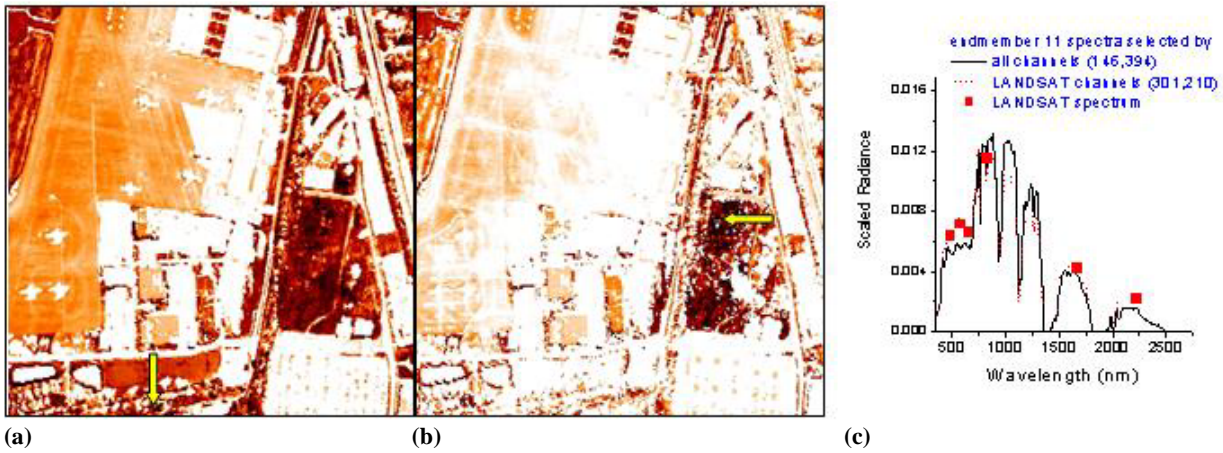**(a)**   **(b)**   **(c)**

Figure 13. Abundance maps derived from the full 224-channel calculations and the 6-channel calculations for endmember pairs (11) are in Figure 13a, 13b respectively. Arrows on the abundance maps point to pixel locations of the selected endmembers. The normalized radiance spectra of the endmember pairs are in Figure 13c.

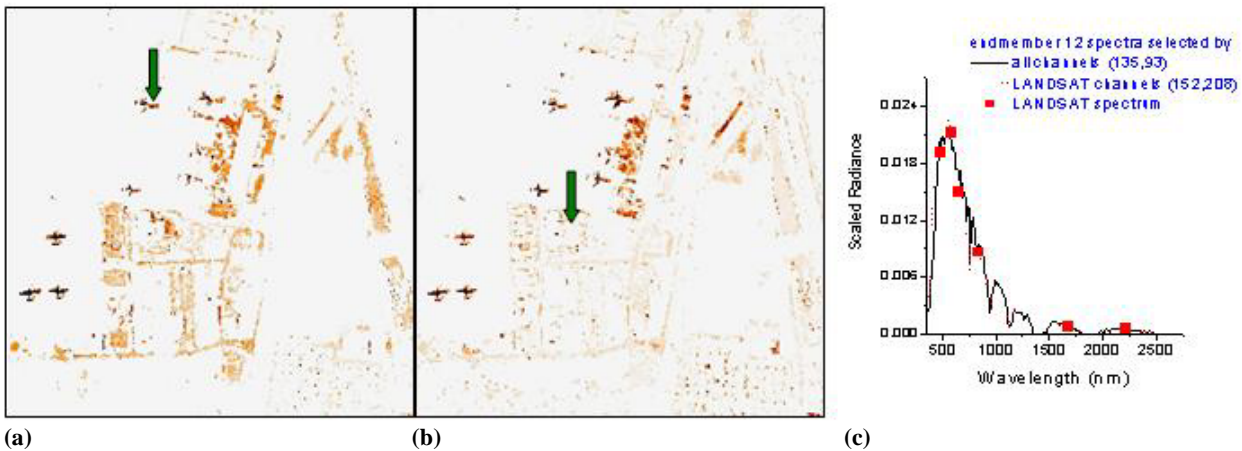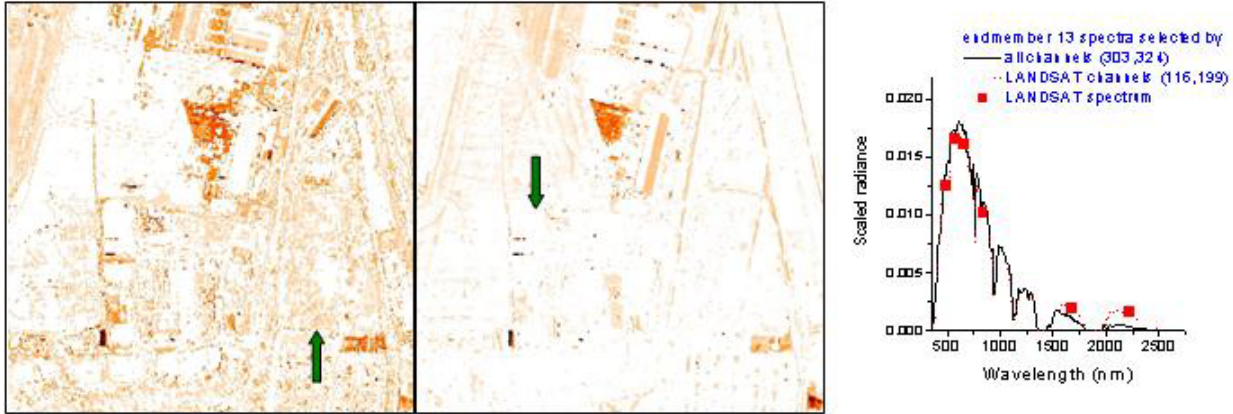**(a)**   **(b)**   **(c)**

Figure 14. Abundance maps derived from the full 224-channel calculations and the 6-channel calculations for endmember pairs (12) are in Figure 14a, 14b respectively. Arrows on the abundance maps point to pixel locations of the selected endmembers. The normalized radiance spectra of the endmember pairs are in Figure 14c.
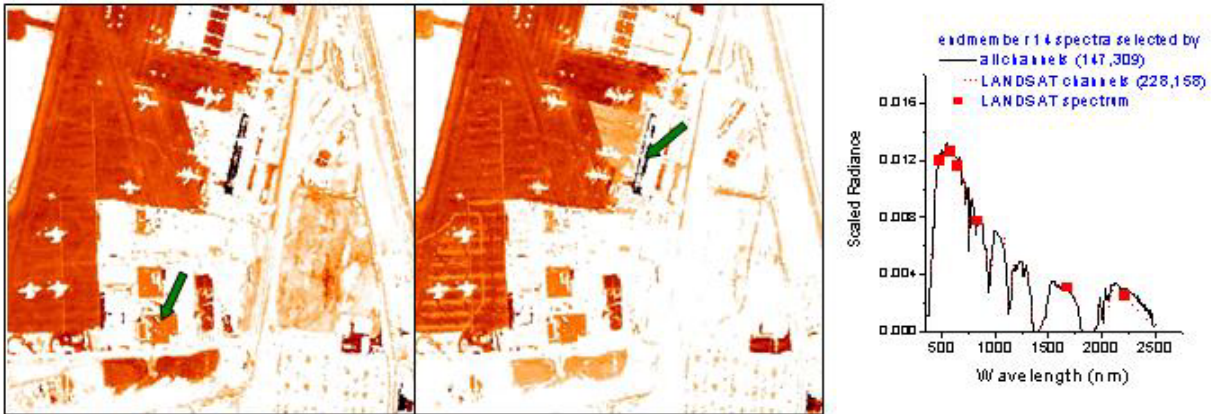
(a)   **(b)**   **(c)**

Figure 15. Abundance maps derived from the full 224-channel calculations and the 6-channel calculations for endmember pairs (13) are in Figure 15a, 15b respectively. Arrows on the abundance maps point to pixel locations of the selected endmembers. The normalized radiance spectra of the endmember pairs are in Figure 15c.

(a)   **(b)**   **(c)**

Figure 16. Abundance maps derived from the full 224-channel calculations and the 6-channel calculations for endmember pairs (14) are in Figure 16a, 16b respectively. Arrows on the abundance maps point to pixel locations of the selected endmembers. The normalized radiance spectra of the endmember pairs are in Figure 16c.

(a)   **(b)**   **(c)**

Figure 17. Abundance maps derived from the full 224-channel calculations and the 6-channel calculations for endmember pairs (15) are in Figure 17a, 17b respectively. Arrows on the abundance maps point to pixel locations of the selected endmembers. The normalized radiance spectra of the endmember pairs are in Figure 17c.

The abundances for the 224-channel and 6-channel calculations of the seventh endmember pair is illustrated in Figures 9a and 9b, respectively. The pixels selected by both calculations are on an object or objects to the right of the cargo storage building. The 224-channel calculation selects pixel (245,148) while the 6-channel calculation selects pixel (245,150). The spectra, illustrated in Figure 9c, differ primarily in the visible with the pixel (245,148) being much more reddish in color. The abundance maps are qualitatively similar; however, the endmember plays a more dominant role in the modeling of the right side of the scene in the 224-channel calculations. Another difference is in the modeling of the aircraft. The 6-channel endmember plays a strong role in modeling the aircraft. The abundances for the eighth endmember pair are illustrated in Figure 10a and 10b. The pixels selected were adjacent, pixel (214,299) for the 224-channel calculation and (213,299) for the 6-channel calculation. The endmember pair spectra are illustrated in Figure 10c. The spectra show that the object is yellow in the visible. It is located to the right of the cargo storage building. Interestingly, this endmember is a major contributor to the pixels on the painted lines on the tarmac. The abundances for the ninth endmember pair are illustrated in Figures 11a and 11b. In this case the pixels are not closely located. The spectra for this endmember pair are illustrated in Figure 11c. The spectra show that the objects in the pixels are blue in the visible. The pixel selected by the 224-channel calculations (233,261) is a blue object to the right of the large light-colored building in the lower central region of the scene. The pixel selected by the 6-channel calculation, (356,353), is a bluish object in the large parking lot in the lower right region of the scene. The pixels contribute to models of several objects as well as paving. Note that this endmember is a contributor to the partially illuminated right side of the cargo storage building in the 6-channel calculations, while the full 224-channel model uses the endmember in the sixth pair.

The abundances for the 224-channel and 6-channel calculations of the tenth endmember pair are illustrated in Figures 12a and 12b, respectively. Different pixels are selected by each calculation. The 224-channel calculation selects pixel (72,358) while the 6-pixel calculation selects pixel (14,361). The endmember pair spectra are illustrated in Figure 12c, showing the pixels to be blue in the visible. The abundance maps show that the endmembers model two regions in the lower left area of the scene. The 224-channel calculation selects a pixel in the rightmost region as endmember while the 6-channel calculation selects one from the leftmost region. The abundance maps for the eleventh pair of endmembers are illustrated in Figures 13a and 13b. The 224-channel calculation selects pixel (146,394) as the endmember, while the 6-channel calculation selects pixel (301,210). (146,394) is at bottom to the left of central under the two light-colored regions below the terminal buildings. Pixel (301,210) in the area to the right of the terminal buildings above the parking lot. Both pixels are dark in the visible. Their spectra are illustrated in Figure 13c and are very similar. These pixels are used to model areas of vegetation, particularly the area to the right of the terminal buildings above the parking lot. While a minor contributor to models of the tarmac and the light-colored regions below the terminal buildings, in both calculations these features are more pronounced in the 224-channel endmember abundances than in the 6-channel endmember abundances.

The abundance maps for the 224-channel and 6-channel calculations of the twelfth endmember pair is illustrated in Figures 14a and 14b, respectively. The 224-channel calculation selects pixel (135,93) as an endmember. This pixel is on the partially illuminated side of the fuselage (wing) of an aircraft in the upper central part of the tarmac. Pixel (152,208) is in the notch above the "L" shaped structure. It appears to be partially shadowed by the structure. The abundance maps are very similar as are the spectra illustrated in Figure 14c. Figures 15a and 15b illustrate the abundance maps for the thirteenth endmember pair. Figure 15c illustrates the spectra. The pixel selected by the 224-channel calculation is a light-colored object in the upper edge of the parking lot on the lower right side of the scene. The pixel selected by the 6-channel calculations is a light-colored object on the edge of the tarmac to the left of the L-shaped building in the center of the scene. This endmember contributes to a large number of small bright objects in the scene as well as to a bright Section of tarmac along a side of the cargo storage building.

Abundance maps and spectra for the fourteenth and fifteenth endmember pair are illustrated in Figures 16 and 17. The abundance maps for the fourteenth pair are very similar. The pixels selected as endmembers are again from different regions of the scene. Pixel (147,309), chosen by the 224-channel calculation, is a small white object to the right of the terminal building. Pixel (228,158), chosen by the 6-channel calculation, is a pixel on the fully illuminated left side of the roof of the cargo storage building. The abundance maps show strong similarity. The abundance maps for the 15th endmember pair are less similar The 6-channel selected endmember models both the fully illuminated left side and partially illuminated right sides of the cargo storage building roof. The 224-channel calculation selected a pixel (238,123) on the partially illuminated right side of the roof of the cargo storage building. It should be noticed that the pixel location of the fifteenth endmember pair of the 6-channel calculation is the same pixel location (147,309) as the

224-channel endmember of the fourteenth pair. The 6-channel calculation is unable in this case to distinguish between the left and right side of the roof, that has slight variations in illumination of the same material. The spectra of all three pixels are all fairly similar; however, pixel (228,158) is the brightest of the three in the visible spectrum. The spectra of the pixels (147,309) and (238,123) differ primarily in the near-IR. (The 224-channel calculation selects an additional endmember with pixel location (225,166) on the left side of the roof of the cargo storage building This endmember is used exclusively in the full-channel models of the left side of the roof. Its spectrum is nearly identical to that of (228,158), the pixel chosen from the left side of the roof by the 6-channel calculation. There is no corresponding additional endmember selected by the 6-channel calculation. The subtle differences in spectral shape in the near-IR are not characterized well enough by the 6-channel spectra to make the same distinctions as the 224-channel calculations in the case.

The remaining endmembers in both calculations contribute to modeling small local variations in the large features of the scene, providing models for sets of spectrally similar isolated small objects in the scene such as cars. The later endmembers and abundance maps are of interest in as candidate target pixels for detection algorithms. The endmembers and pixels modeled by them have anomalous spectral features. Further investigation is required to make a detailed determination of the similarities of the full-channel and six-channel selections of anomalous pixels.

4. CONCLUSIONS

Our convex approach with constraints requiring positive abundances and constraint on the maximum number of endmembers for a pixel model provides a detailed physical description of hyperspectral and multispectral imagery data. Environmental and illumination variations can be included in the mixing models and the number of endmembers is not limited by the number of channels or bands of the sensor. Materials and their spectral variations induced by environmental and illumination variations are modeled with scene spectra that are extracted as endmembers. The approach leads to multiple mixing models with subsets of the endmembers representing the materials in the scene and provides detailed spatial distributions. Endmembers, pixel models and abundances are determined simultaneously and autonomously. The method provides a unique processing capability for multispectral data.

ACKNOWLEDGEMENTS

REFERENCES

1. J.H. Gruninger, A.J. Ratkowski and M.L. Hoke, "The Sequential Maximum Angle Convex Cone (SMACC) Endmember Model." *Proceedings SPIE, Algorithms for Multispectral and Hyper-spectral and Ultraspectral Imagery X*, Orlando, April (2004).
2. A.C. Bateson, G.P. Asner and C.A. Wessman, "Endmember Bundles: A New Approach to Incorporating Endmember Variability into Spectral Mixture Analysis," *IEEE Transactions on Geosci. and Remote Sensing*, **38**, 1083-1094, (2000).
3. J.H. Gruninger, M.J. Fox and R.L Sundberg, "Hyperspectral Mixture Analysis Using Constrained Projections onto Material Subspaces," *Proceedings International Symposium on Spectral Sensing Research (ISSSR),* Quebec City , pp 162-170, June 11-15 (2000).
4. D.W.J. Stein "Application of the Normal Compositional Model to Hyperspectral Imagery," *IEEE Workshop on Advances Techniques for Analysis of Remotely Sensed Data*, Greenbelt Maryland , October, (2003).
5. F. Maselli "Multiclass Spectral decomposition of remotely Sensed Scenes by Selective Pixel Unmixing," *IEEE Transactions on Geoscience and Remote Sensing,* **36**, pp1809-1820, (1998).
6. G.D. Robinson, H.N. Gross and J.R. Schott, "Evaluation of Two applications of Spectral Mixing Models to Image Fusion," *Remote Sens. Environ.* **71**, 272-281 (2000).
7. J. Bowles, M. Daniel, J. Grossman, J. Antoniades, M. Baumback and P. Palmadesso, "Comparison of Output from ORASIS and Pixel Purity Calculations," *Proc. SPIE Imaging Spectroscopy IV*, **3438**, pp 148-156, San Diego July 19-24 (1998).

8. M.E. Winter, "N-FINDR: An Algorithm for Fast Autonomous Spectral Endmember Determination in Hyperspectral Data," *Proc. SPIE Imaging Spectroscopy V*, **3753**, 266-275, Denver July (1999).

9. R.A. Neville, K. Staenz, T. Szeredi, J. Lefebvre, and P. Hauff, "Automatic Endmember Extraction from Hyperspectral Data for Mineral Exploration*," Proceedings of the Fourth International Airborne Remote Sensing Conference and Exhibition / 21st Canadian Symposium on Remote Sensing*, Vol. **II**, 891-897, Ottawa, Ontario Canada 21-24 June (1999).

10. M.E. Winter and E.M. Winter, "Comparison of Approaches for Determining Endmembers in Hyperspectral Data" *Proc. IEEE Aerospace Conference*, Big Sky Montana, March 18-25 (2000).

11. J.W. Boardman, "Analysis, understanding and Visualization of Hyperspectral data as Convex Sets in n-space," *Proc SPIE, Imaging Spectroscopy,* **2480** pp 14-22, Orlando April (1995)

12. M.D. Craig, "Minimum-Volume Transformations for Remotely Sensed Data," *IEEE Trans. Geoscience and Remote Sensing,* **32**, 99-109, (1994).

13. D.R. Fuhrmann, "A Simplex Shrink-wrap algorithm," *Proc. SPIE AeroSense ATR IX*, **3718** 155-166, Orlando April (1999).

14. P. Palmadesso, J. Antoniades, M. Baumback, J. Bowles and L. J. Rickard, "Use of Filter Vectors and Fast Convex Set Methods in Hyperspectral Analysis" *ISSSR*, Australia, November (1995).